ELECTRONIC SUPPLEMENTARY MATERIALS

Jan W. Kruyt[1,2], GertJan F. van Heijst[3], Douglas L. Altshuler[4], David Lentink[1]*

[1]Mechanical Engineering, Stanford University, 416 Escondido Mall, Stanford, CA 94305, USA.

[2]Experimental Zoology Group, Wageningen University, P.O. Box 338, 6700 AH, Wageningen, The Netherlands.

[3]Physics Department, Eindhoven University of Technology , P.O. Box 516, 5600 MB, Eindhoven, The Netherlands.

[4]Department of Zoology, University of British Columbia, #4200-6270 University Blvd, Vancouver, BC V6T1Z4, Canada.

Animals. Seven male Anna's hummingbirds (*Calypte anna*), euthanized for other studies at the University of California, Riverside, were stored frozen in good condition. After careful preparation, their wings were donated to the Museum of Vertebrate Zoology at the University of California, Berkeley, and subsequently loaned from the University of California, Berkeley (CITES: US-052 (A/P)) to Wageningen University (CITES: NL-004) for aerodynamic study. The wings originated from birds for which all animal procedures were approved by the Institutional Animal Care and Use Committee of the University of California, Riverside.

Wing preparation. The hummingbird wings were removed from the (proximal) base of the humerus and dried in fully spread position to resemble wing morphology during hovering flight. We removed minimal amounts of wing material to glue the wing base into a square plastic tube aligned with the innermost secondary feather. The square tube was mounted on a square rod attached to the variable pitch mechanism of the spinner. We then selected $n = 5$ right wings that had least imperfections in the feathers due to wear, molt, and preparation, Supplementary Figure 1a. Each wing's out-of-center mass was carefully counterbalanced with an opposing plastic mount filled with lead fishing weights. Finally, we artificially groomed (preened) the feathers with our fingers and an entomological pin to close small gaps. When necessary gaps were closed using a minimal amount of hairspray applied locally with a pin; we sprayed the solution in a cup, soaked the head of the pin in it, and applied minimal amounts with the pin to fix particular barbs.

Model wing design. We confirmed similarity of the aerodynamic performance of rectangular model wings (AR = 3.5, *Re* = 11,000) and *Calypte anna* wings (n = 5, ave *A*R = 4.1, ave midstroke *Re* = 14,000), figure 1c. To isolate the effect of aspect ratio on revolving wing performance, we then designed a range of carbon fiber model wings. These wings vary in wing length only and have the same rectangular planform, constant chord length, and camber, supplementary figure 2. A recent analysis[1] predicts that stall delay on revolving wings is mediated by rotational accelerations, and that stabilization of the leading edge vortex (LEV) stops beyond a local aspect ratio r/c (local radius, r, divided by chord, c) between 1 and 10, close to 3. We selected aspect ratios (*A*R = 2-3-4-5-6.5-8-10) that sample this range and the hummingbird aspect ratio range: *A*R = 3.7 ± 0.3 *std* (n = 65). The model wings were built up from two 0.2mm carbon fiber plies and had 15mm chord. We selected 6% airfoil camber for good hover performance[2-4], similar to hummingbird wings[5]. We iterated the airfoil design to ensure the wing was stiff enough and did not flutter within our measurement range. Each wing was fitted with a plastic square mount to clamp it onto the spinner and a minimally protruding hooklet at the wing base. This hooklet helped secure each model wing to the spinner with an orthodontic rubber band. We found that hummingbird wings and low aspect ratio model wings could be spun without vibration by balancing them using a counterweight (fishing leads attached to plastic mount). High aspect ratio model wings, however, vibrated due to the relatively large eccentric aerodynamic forces at the larger outward radius of gyration of the wing[6]. We therefore tested all model wings in pairs, which balances the aerodynamic and inertial forces such that the setup does not vibrate. Each wing pair was carefully balanced by gluing small lead fishing weights at the lower surface into one of the plastic mounts.

Wing spinner. We designed a computer-run wing spinner to autonomously control wing tip Reynolds number, *Re*, (through spinning frequency) and incidence angle, α, of single wings or wing pairs. Two micromotors (AXi2212/34 and AXi2208/20, Model Motors) with complementing torque ranges powered a single hollow axle, suspended with ball bearings in an aluminum housing. Through the axle ran a non-rotating, servo-actuated push-pull rod to control a variable pitch propeller mechanism fitted with square rods on which the plastic wing mounts could be clamped. The micromotors were controlled using an electronic speed controller (M-Drive-18, Motortron System Inc) and a servo board (ServoCenter 3.1, Yost Engineering). The spinner design minimized the distance between the rotation axis and the wing root, d, to 9.5mm. This offset was incorporated in our calculation of the target spinning frequencies to maintain constant wing tip Reynolds number $Re = \rho 2\pi f(R + d)c/\mu$ (air density, ρ, spinning frequency, f, wing length, R, and dynamic viscosity, μ). The dynamic viscosity was calculated based on the measured air temperature using Sutherland's equation[7]: $\mu = \mu_0 \, (T_0/T)^{1.5} \, (T_0 + S)/(T + S)$, (air temperature, T, μ_0 = 18.27ms^{-2}, T_0 = 291K, Sutherland's constant for air, S = 120K). The same spinner was used during force measurements and quantitative flow visualization.

Calibration of force measurement. To make reliable static (time-averaged) force measurements, the spinner was mounted onto an overdamped balancing setup supported by weighing scales (Ohaus Adventurer Pro, 210g range, ±0.001g), Supplementary Figure 1c. Accuracy of the torque measurement proved to be the setup's main challenge, as expected based on earlier studies[8,9], and was improved greatly by automating the setup, thus minimizing the required handling between measurements. Accuracy was further improved by mechanically isolating the setup on a heavy granite table supported by rubber dampers, and aerodynamically shielding the balance from the propeller wake with clear plastic cowlings rested on separate supports, Supplementary Figure 1b, c. High-frequency vibrations from the spinner were damped using rubber-plated motor suspension and averaged out using custom-built silicon oil dampers (10,000 cSt polydimethylsiloxane, Tribolub). We calibrated the force balance statically by using weights to apply lift force along the rotation axis (0.3° accuracy) and pure torque around the rotation axis. These weights were hung from wires running horizontally from the setup over pulleys with negligible friction. We applied a pure torque (without net force) by mounting a vertical arm, sticking both upward and downward, onto the spinner. One wire was connected to the upper end of the arm and another wire in the opposite direction to the lower end, to apply identical but opposing forces, resulting in a pure torque. All weights were submerged in paraffin oil (2.4 cSt, Texaco) to prevent them from swaying during the calibration. To account for coupling effects, we applied combinations of lift and torque to build a 9×9 calibration matrix with increased resolution around zero lift and torque to accomodate low Reynolds number measurements. These calibrations were repeated five times before and after the measurements. Average calibration bias over all measurement points was 5.0% on torque and 1.0% on lift. We separately measured lift and torque generated by the rotating parts, e.g. mechanical friction in the ball bearings and aerodynamic drag on the plastic wing mounts, as well as center of gravity displacement due to servo actuation, and subtracted all these effects from the wing measurements to obtain precise aerodynamic forces.

Force measurements. We measured time-averaged lift and torque on wings spinning at constant Reynolds number and incidence. After a conservative 5 second settling period (determined experimentally), the measured reaction forces were sampled 100 times via USB at 5-6Hz and stored by custom-built Matlab code (v2009a, Mathworks). Thin wires were connected close to the balance's central pivoting point for power supply (7.4VDC, DPS-2010PFC, Voltcraft) and motor control. The model wings were taken through a range of Reynolds numbers (*Re* = 5,000-25,000, stepsize 4,000) and incidence angles ($\alpha = -3°$-60°, stepsize 1° for $\alpha < 20°$ and 3° for $\alpha \geq 20°$). Hummingbird wings were tested at the midstroke Reynolds number during hover (ave *Re* = 14,000) calculated using measured mean chords and angular velocities assuming a sinusoidal wing stroke[6]. The aerodynamic measurements were repeated 3 times. Every repetition consisted of an upward leg during which incidence was increased till the maximum angle of attack was attained, after which the angle of attack was reduced during the downward leg till it reached the minimum value. These three complete loops enabled us to check for hysteresis effects, which we did not find. The weighing scales measured lift forces ranging between 0.00003N and 5.73N and torques between 0.000013Nm and 0.246Nm. The torque measurement range was limited by motor power (at very high and very low *AR*, *Re,* α) and by measurement resolution (at very low *AR*, *Re,* α). We obtained 600 measurements per data point for statistical rigor. Since the setup has been calibrated for static measurements, resulting in a static transfer function that relates displacement to force, we checked if the balance attained static conditions. We used the fast Fourier transform (FFT) to compute the dynamic power present in the frequency spectrum below 1Hz (at higher frequencies the power was negligible) in both the lift (Supplementary Figure 3a, c, e.) and torque (Supplementary Figure 3b, d, f.) measurements. Based on this evaluation we disregarded the torque measurements for which the balance was unable to reach static equilibrium: at *Re* =5,000 and beyond 35° incidence (Supplementary Figure 3b, d, f.). All lift measurements were static and thus accepted, Supplementary Figure 3a, c, e. A single outlying point for the drag coefficient was marked as a dot, Supplementary Figure 4b, 5b, but removed from the Reynolds average (Figure 2).

Force coefficients. We calculate aerodynamic force coefficients by dividing lift by $1/2\,\rho(2\pi f)^2 S{R_2}^2$ and drag due to torque by $1/2\,\rho(2\pi f)^2 S{R_3}^3$ using air density, ρ, spinning frequency, f, wing area, S, and the radii of second and third moments of area R_2 and R_3, to account for the velocity gradient along the wing span[6,8]. Lift is defined as the force perpendicular to the stroke plane, neglecting induced flow effects. After checking for hysteresis effects, which we did not find, we averaged the 600 lift (C_L) and drag (C_D) coefficients measured at each incidence. Zero incidence was defined as the point of zero lift, based on the zero intercept of the C_L-α curve for $0.05 \leq C_\mathrm{L} \leq 0.50$ for each wing.

Power factor. To compare the aerodynamic power required for hover we compute power factor as a function of incidence, $PF = C_\mathrm{L}^{1.5}/C_\mathrm{D}$. The amount of weight that can be lifted with a unit aerodynamic power is proportional to this factor[10]. Power factor represents a 'gradient' and therefore amplifies noise in the drag coefficient. A penalized least-squares algorithm[11] was used to smooth the force coefficient curves versus incidence before calculating the power factor and thus limit noise.

Particle image velocimetry (PIV). To quantify the velocities in the flow around the wings, we seeded the room with microscopic smoke particles illuminated by laser light captured with a phase locked camera (details are provided in Supplementary Table 1 below). We recorded 20 (model wings) or 25 (hummingbird wings) phase-locked image pairs in 2D planes along the span of the spinning wing. We automatically moved the imaging plane along the span using a linear actuator that traversed the spinner and its mounted wing through a laser sheet. Both the laser and the PIV camera were triggered when the wing passed in front of a camera, Supplementary Figure 1b, d. The laser beam was split using mirror optics to illuminate the wing and reduce shadow effects. Image pairs were cross-correlated using DaVis software (v7.4, LaVision GmbH) using a multi-pass cross-correlation procedure consisting of a first pass on a 128×128 pixel grid (0% overlap) and then two passes on a finer 64×64 pixel grid (75% overlap)[12]. Flow measurements were made for all model wings over a range of Reynolds numbers (Re = 5,000-13,000-25,000) and incidence angles (α = 15°-30°-45°). One wing of *Calypte anna* was tested at its midstroke Reynolds number (Re = 13,000) at these same three incidence angles. We made recordings at 19-22 equidistant spanwise recording stations from wing root to well beyond the tip. Step sizes for the model wings increased from 1.3 to 6.6 mm with aspect ratio; step size was 2.25 mm for the hummingbird wing. Reflections from the spinner as well as the plastic wing mounts were minimized using matte black grease (Zebraline stove polish), and the model wings were coated with matte black spray paint. During postprocessing, images from a simultaneously triggered second camera, under a 35° stereo angle, were used to correct for small trigger errors and match airfoil positions precisely to calculate the average flow field.

Vortex identification. The leading edge vortices are visualized by plotting vorticity. We used a vortex detection scheme to confirm that the visually obvious vorticity concentrations are vortices using the MATLAB vortex identification code of Jones *et al.*[13]. This implementation of a non-linear vortex detection scheme in which the axisymmetric vortex intensity at a point P in the velocity field is defined as $\gamma(P) = \frac{1}{N}\sum \sin(\theta_M)$ following the work of Graftieaux *et al.*[14]. This identification method is more robust against noise in the PIV recordings[13]. Vorticity concentration and high vortex identification levels overlap, demonstrating that the vorticity concentration at the leading edge are indeed a leading edge vortex for all wings tested (Supplementary Figure 8). We thus conclude that our vorticity fields are sufficiently noise-free to detect vortices based on vorticity concentration.

Vortex lift coefficient. The vortex lift distribution was calculated by integrating the vorticity field to determine local circulation, Γ, for a fixed control area intersecting the wing at each spanwise station.

We omitted the area below the wing, where the laser illumination was insufficient, from the area of integration. We cut off vorticity below a threshold level based on free-stream vorticity noise measured in front of the wing. From the circulation we computed local vortex lift coefficients as $C_l = 2\Gamma/Vc$ using local wing velocity, V, and chord length, c. For the hummingbird wing we used the local wing chord in this computation. The average vortex lift integrated over the full span of each model wing predicted 78-97% of the lift measured with the force balance for model wings at α = 30°, and 55%-109% at 45°; for the hummingbird wing the calculated fraction was 71% of the measured lift coefficient at 30° and 77% at 45°. The discrepancy between measured and calculated lift is expected, because the control volume integral of the Navier-Stokes equations is only approximated by integrating circulation[12,15-22].

Table 1. Components of phase-locked PIV setup

Smoke generator	VDP900HZ, HQ power
Laser	Dual SL454-10-OPG, Spectron Laser Systems, flashlamp pumped Nd:YAG laser, 532nm, 200mJ/pulse, 13ns pulse duration, 15Hz repetition rate
Tachometer for triggering	PLT200, Monarch Instrument
Camera	MegaPlusII ES 2020, Redlake, 30fps, 1600x1200px with 105mm zoomlens, Nikkor Micro, Nikon
Linear actuator	custom design, 5mm/stroke ball screw, AMS AM34-420-2-EFB stepper motor and AMS MAX-410 controller

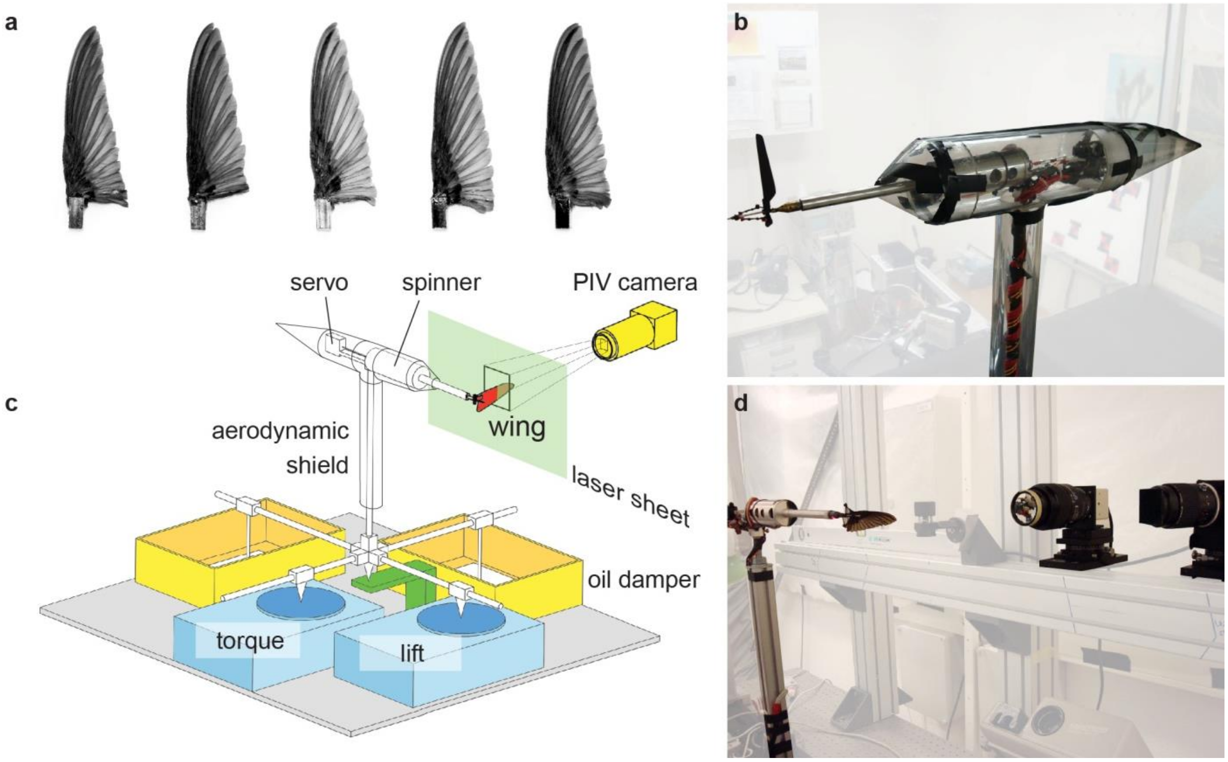

Figure S1. Hummingbird wings and spinner setup used for force measurements and quantitative flow visualizations. (**a**) The right wings of five male Anna's hummingbirds (*Calypte anna*) were used for force measurements; the left-most wing produced a force polar close to the species average and was used during PIV measurements. Each wing is glued into a plastic mount that clamps onto the spinner. (**b, c**) During force measurements the spinner was mounted on a balance pivoting on a fulcrum (green) and supported by weighing scales (blue) to measure reaction forces. The setup's center of gravity deliberately almost coincided with the pivoting point. The counterweight is connected below the fulcrum (not shown here for clarity, it consists of a custom □-shaped aluminum connector that fits around the fulcrum). The balance was overdamped to measure time-averaged forces. The spinner was also carefully shielded from propeller secondary flow using a separately supported cowling (clear plastic). This cowling connected to a bottom plate (not visible) supported by side plates that shielded the balance system from air currents. (**d**) Phase-locked image pairs were recorded by a PIV-camera looking along the wing span during the PIV measurements. A second camera under a 35° stereo angle assisted in determining the wing location in the flow field. The spinner was traversed laterally through the laser sheet using a linear actuator (not visible).

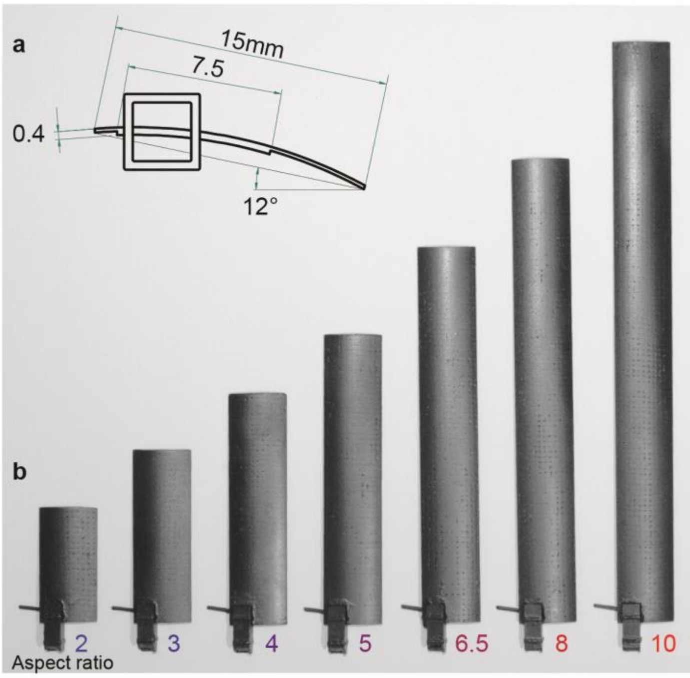

Figure S2. Model wings with aspect ratios 2-10. Carbon fiber model wings were produced by ProxDynamics in Nesbru, Norway and used for force measurements and PIV. All wings were originally produced with aspect ratio 10 with constant chord and uniform airfoil. To lower aspect ratio, wing length was reduced using a table saw with a diamond-tipped blade. (**a**) The airfoil is built up from two 0.2mm carbon fiber plies with 6% camber and 15mm chord length. The airfoil design was iterated to eliminate flutter throughout the measurement range. (**b**) Each wing is glued into a small plastic mount at the quarter-chord point, which clamps onto the spinner. Small carbon fiber rods protruding from the wing base served as hooklets around which we tied small orthodontic rubber bands to secure each wing to the spinner.

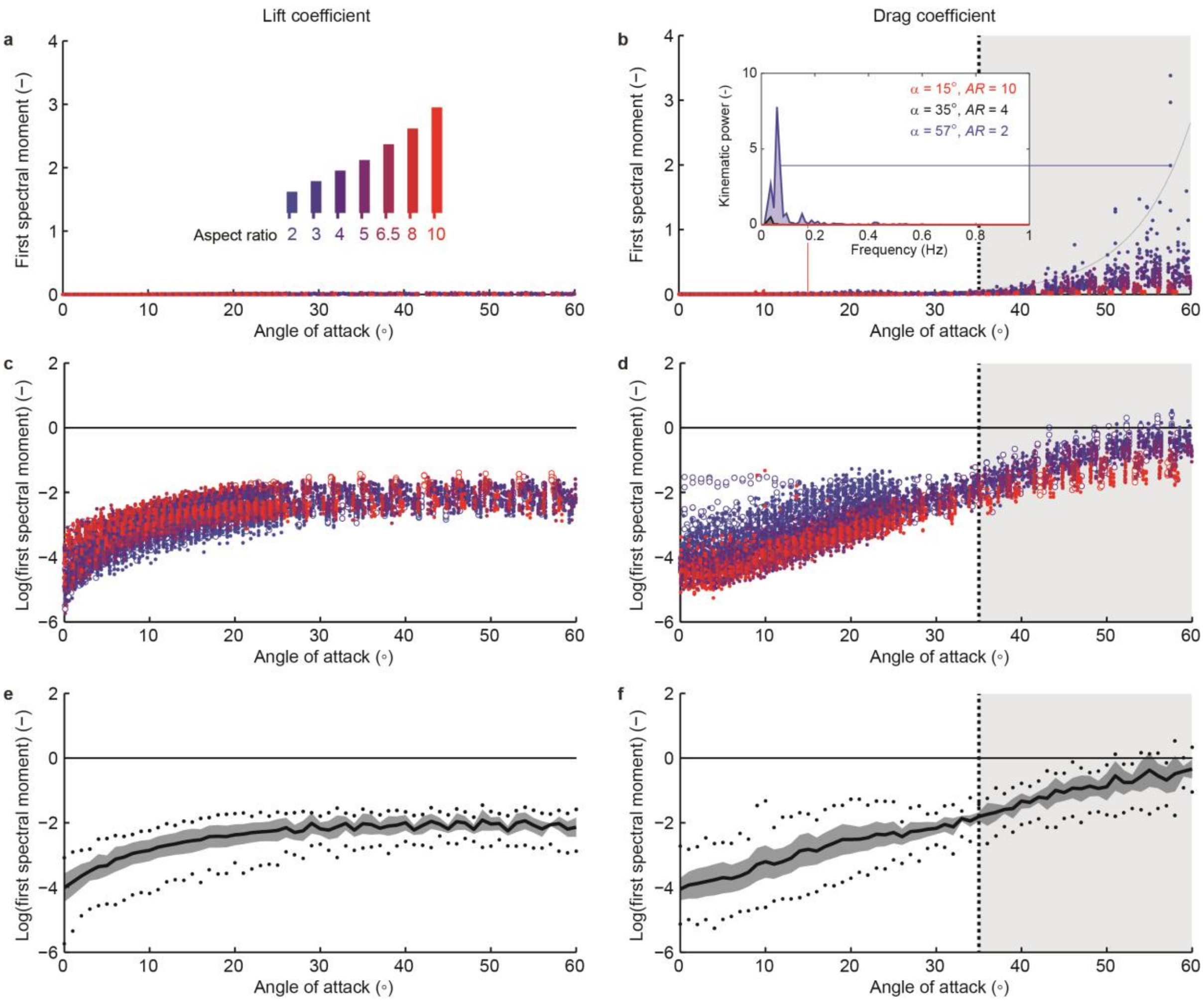

Figure S3. Low frequency fluctuations in the raw drag coefficient signal indicate measurement limitations at *Re* = 5,000 and for α > 35°. The power spectrum of the raw lift (left) and drag (right) coefficient signal (sampling frequency 5-6Hz) was computed using a fast Fourier transform (mean value subtracted; signal reflected at both end points) in the 0-1Hz frequency range, which contained almost all power. We calculated the first spectral moment by integrating power × frequency in this range, which represents a frequency-weighted form of kinematic power. The kinematic power contained in these low frequencies indicates whether system dynamics interfered with measurement of setup deflection, which was calibrated to determine aerodynamic forces. The kinematic power of the force coefficient series is non-dimensional. (**a, c, e**) Average kinematic power in the lift coefficient series does not exceed 0.012 for α=0–60°, indicating all lift force measurements were within the steady range of the balance. (**b**) Kinematic power in the drag coefficient signal is 0.017 ± 0.006 around 35° incidence, and increases exponentially beyond acceptable levels at this angle. This is illustrated by the grey exponential fit through the maximum power at each incidence for 30° ≤ α ≤ 60° ($C_D = 10^{-3.52+0.0656\alpha}$, R^2 = 0.9168). Since the setup was calibrated statically to measure steady forces, we disregarded all drag measurements beyond 35°, because these drag force measurements were within the dynamic range of the balance. The sub-panel shows representative spectra for different angles of attack, above 35° the drag spectra reveal balance dynamics. (**d**) The kinematic power in the drag coefficient signal is highest for low aspect ratio wings at *Re* 5,000 both at low and high incidence. Model wings with aspect ratios 2–4 at Reynolds number 5,000 generate the smallest aerodynamic forces in this dataset, defining the range limitation of the setup. We therefore omitted the measurements at Reynolds number 5,000 from the analysis. Open dots plotted in c,d represent *Re* 5,000; closed dots *Re* 9,000-25,000. (**e, f**) Average logarithmic power for all force coefficient measurements at *Re* ≥ 9,000 (thick black line: average, area: std, dots: min & max values).

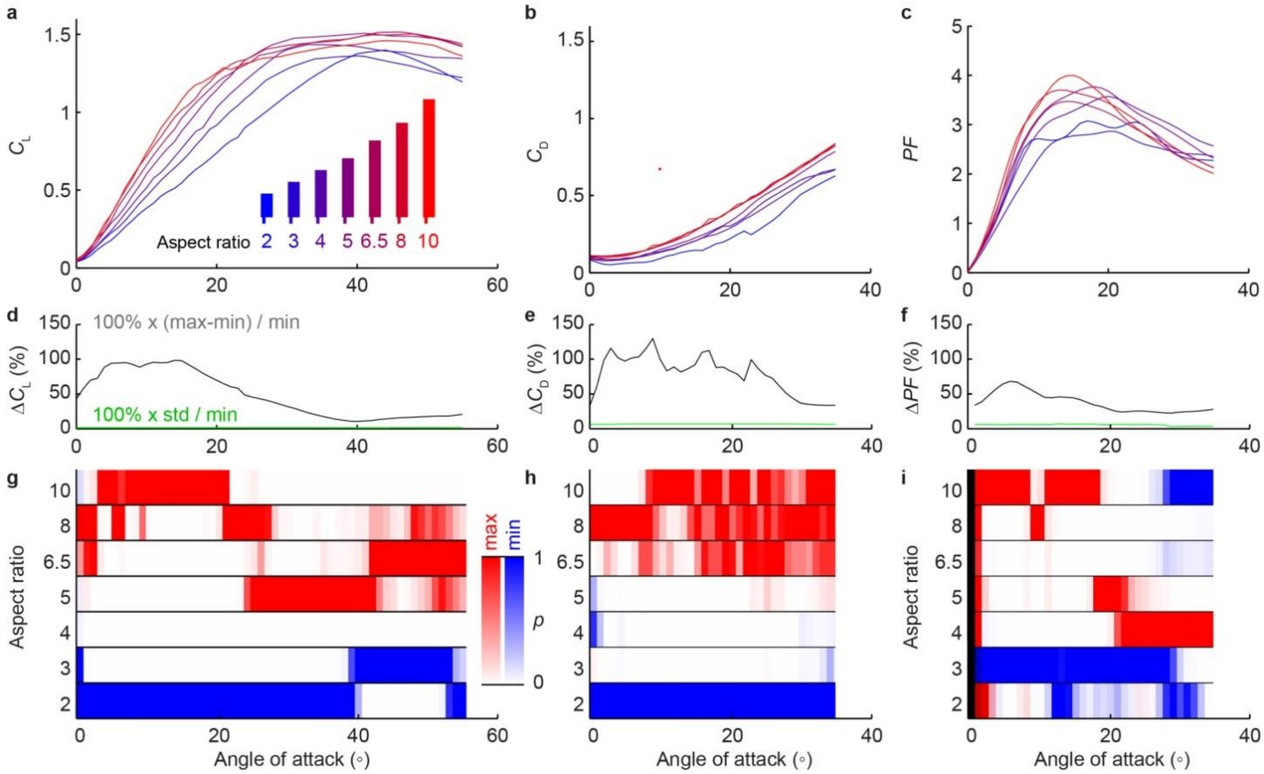

Figure S4. Aspect ratio effect on force coefficients at hummingbird midstroke *Re* = 13,000 is similar to the *Re* averaged effect shown in Figure 2. (**a**-**c**) Lift, drag and power factor versus angle of attack as a function of aspect ratio. Aspect ratio 4 wings combine near maximal lift, and intermediate drag, which maximizes power factor beyond 20°. A single outlying point for the drag coefficient is marked as a dot (and ignored in *Re* average, Figure 2.). The relative difference between minimum and maximum lift (**d**), drag (**e**), and power factor (**f**) among wings is substantial (green line, std calibration accuracy for reference). The optimal aspect ratio to obtain maximum (red) versus minimum (blue) lift (**g**), drag (**h**), and power factor (**i**) depends on incidence. The color intensity corresponds with the p-value of the Wilcoxon rank-sum test for aspect ratio at constant incidence. The effect of aspect ratio on power factor at $\alpha = 0°$ could not be established due to numerical sensitivity to experimental error near zero lift, which produced outliers that were disregarded (vertical black area at $\alpha = 0°$).

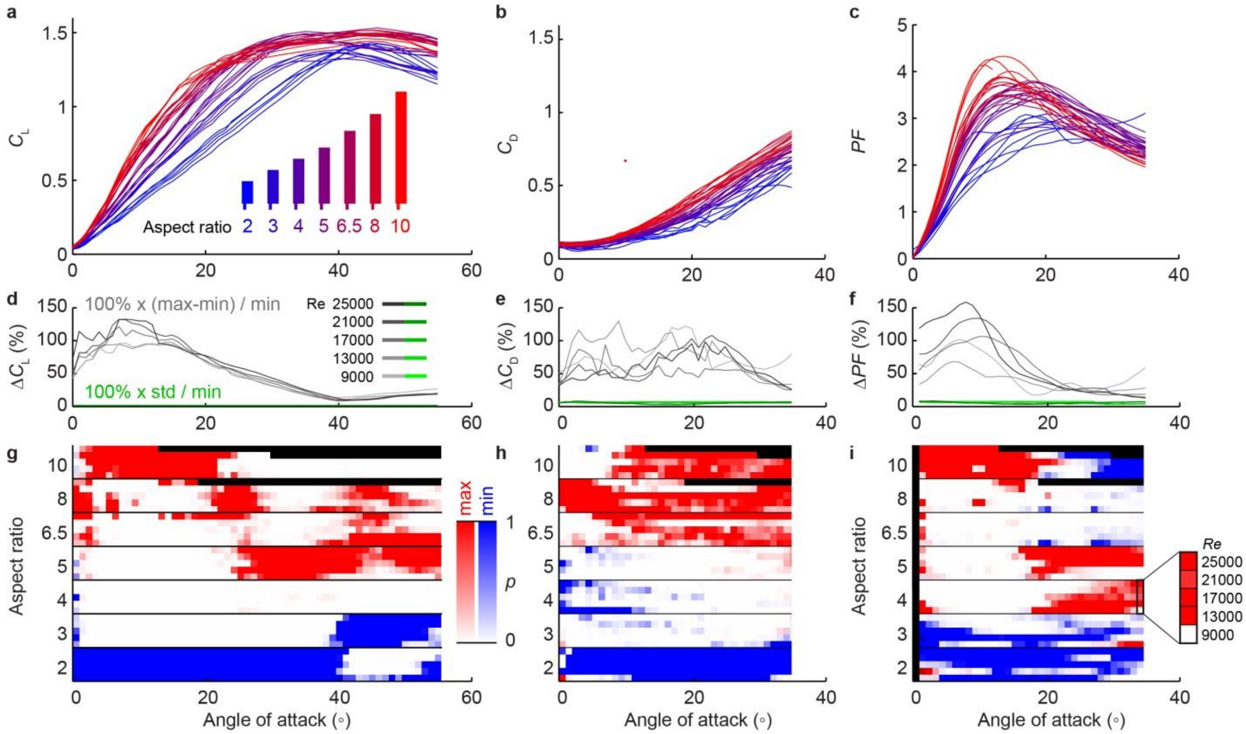

Figure S5. Reynolds number has limited effect on force coefficients across *Re* = 9,000-25,000. (**a**-**c**) Lift, drag and power factor versus angle of attack as a function of aspect ratio. Aspect ratio 4 and 5 wings combine near maximal lift, and intermediate drag, which maximizes power factor beyond 20°. A single outlying point for the drag coefficient is marked as a dot. The relative difference between minimum and maximum lift (**d**), drag (**e**), and power factor (**f**) among wings is substantial (green line, std calibration accuracy for reference). The optimal aspect ratio to obtain maximum (red) versus minimum (blue) lift (**g**), drag (**h**), and power factor (**i**) depends on incidence. The color intensity corresponds with the p-value of the Wilcoxon rank-sum test for aspect ratio at constant incidence. Motor power limited the achievable incidence range for aspect ratio 8 and 10 wings at *Re* = 21,000-25,000 (horizontal black areas). The effect of aspect ratio on power factor at $\alpha = 0°$ could not be established due to numerical sensitivity to experimental error near zero lift, which produced outliers that were disregarded (vertical black area at $\alpha = 0°$).

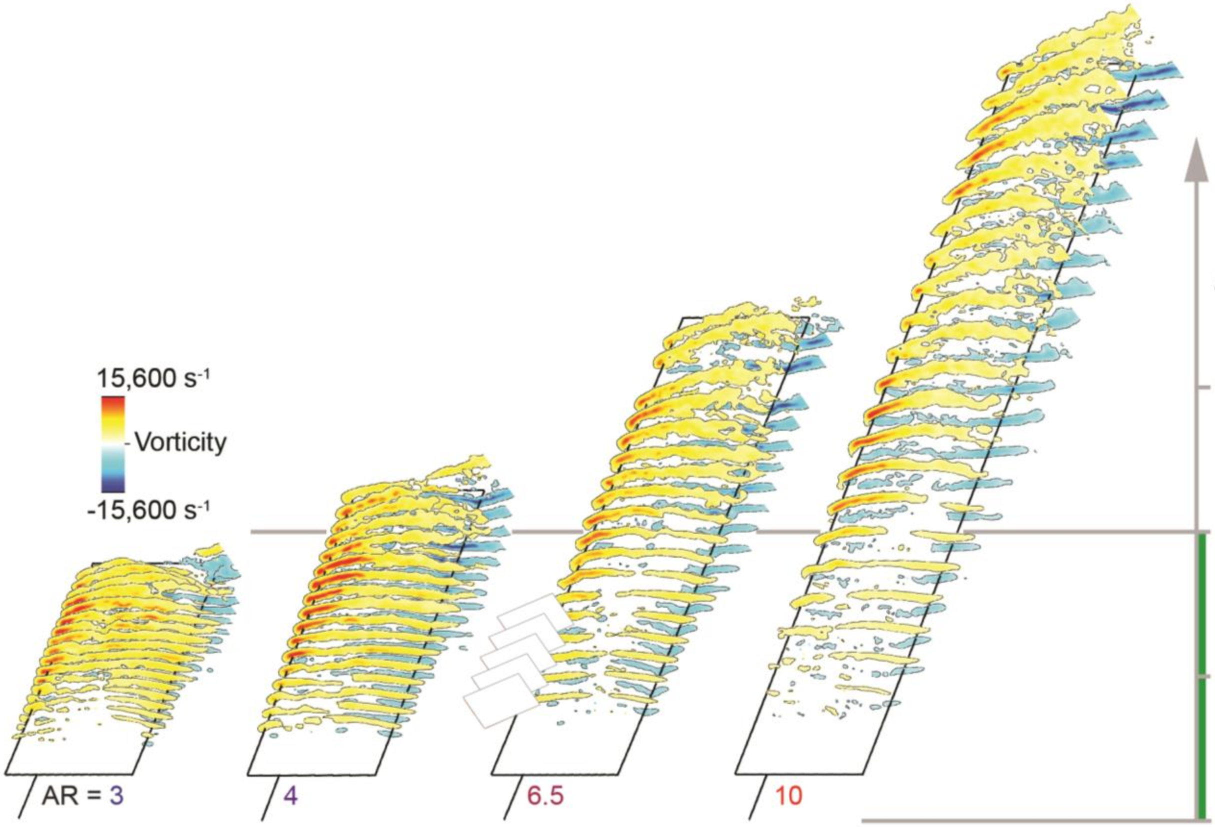

Figure S6. The leading edge vortex remains attached at radii up to 4 chord lengths at 30°. Average vorticity concentration at *Re* = 13,000 reveals an attached leading edge vortex inboard of $r / c \sim 4$. Outboard vortices detach from the leading (yellow, red) and trailing edge (blue). We masked the vorticity field on the inboard leading edge of the aspect ratio 6.5 wing because stove polish proved unsuccessful to reduce background reflections on the plastic wing mount and carbon fiber hooklet in those particular images. One flow field close to the tip of the aspect ratio 6.5 wing was not recorded at 30° and is therefore not shown.

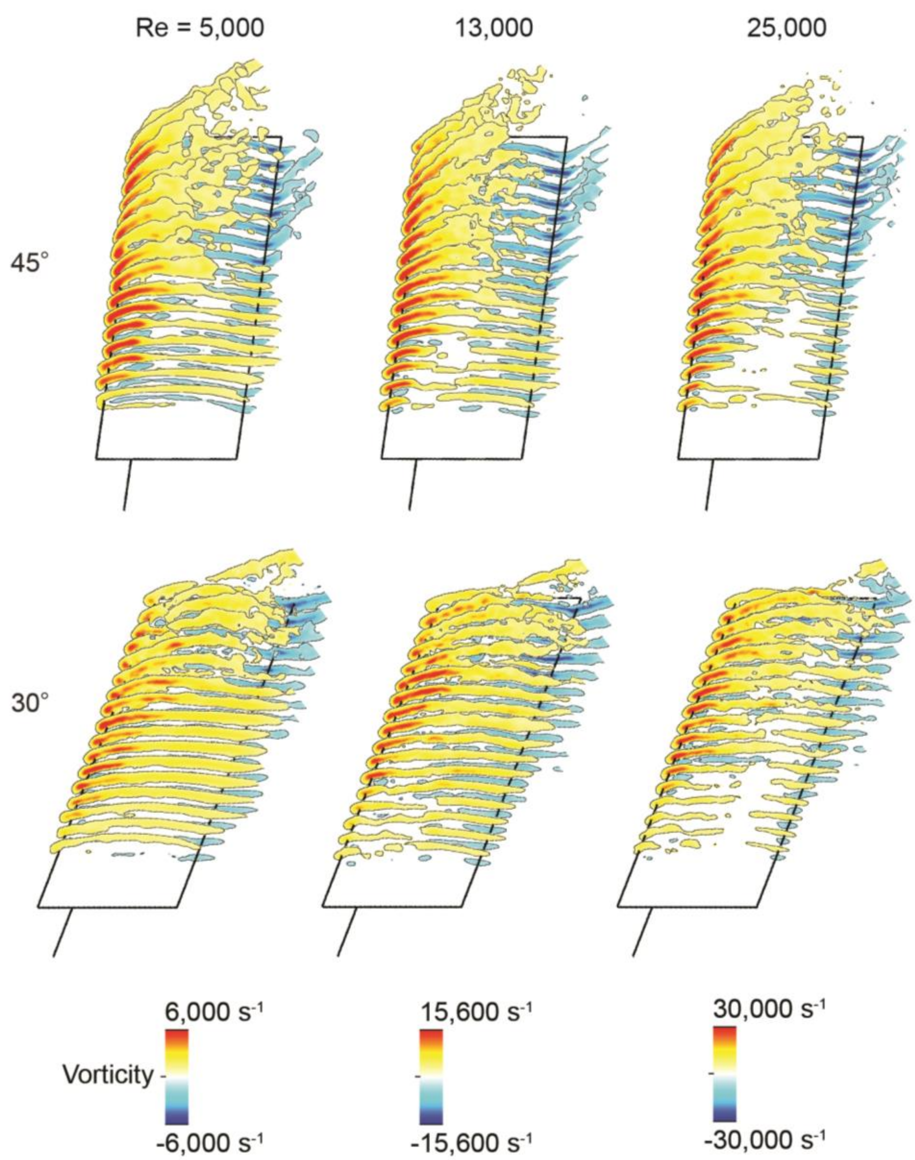

Figure S7. Reynolds number has limited effect on vorticity around an aspect ratio 4 wing across *Re* = 5,000-25,000. Average vorticity concentrations are similar for different *Re*, at both 30° and 45° incidence. A leading edge vortex attached to the inboard wing merges with the tip vortex outboard, as shown for maple seeds [23].

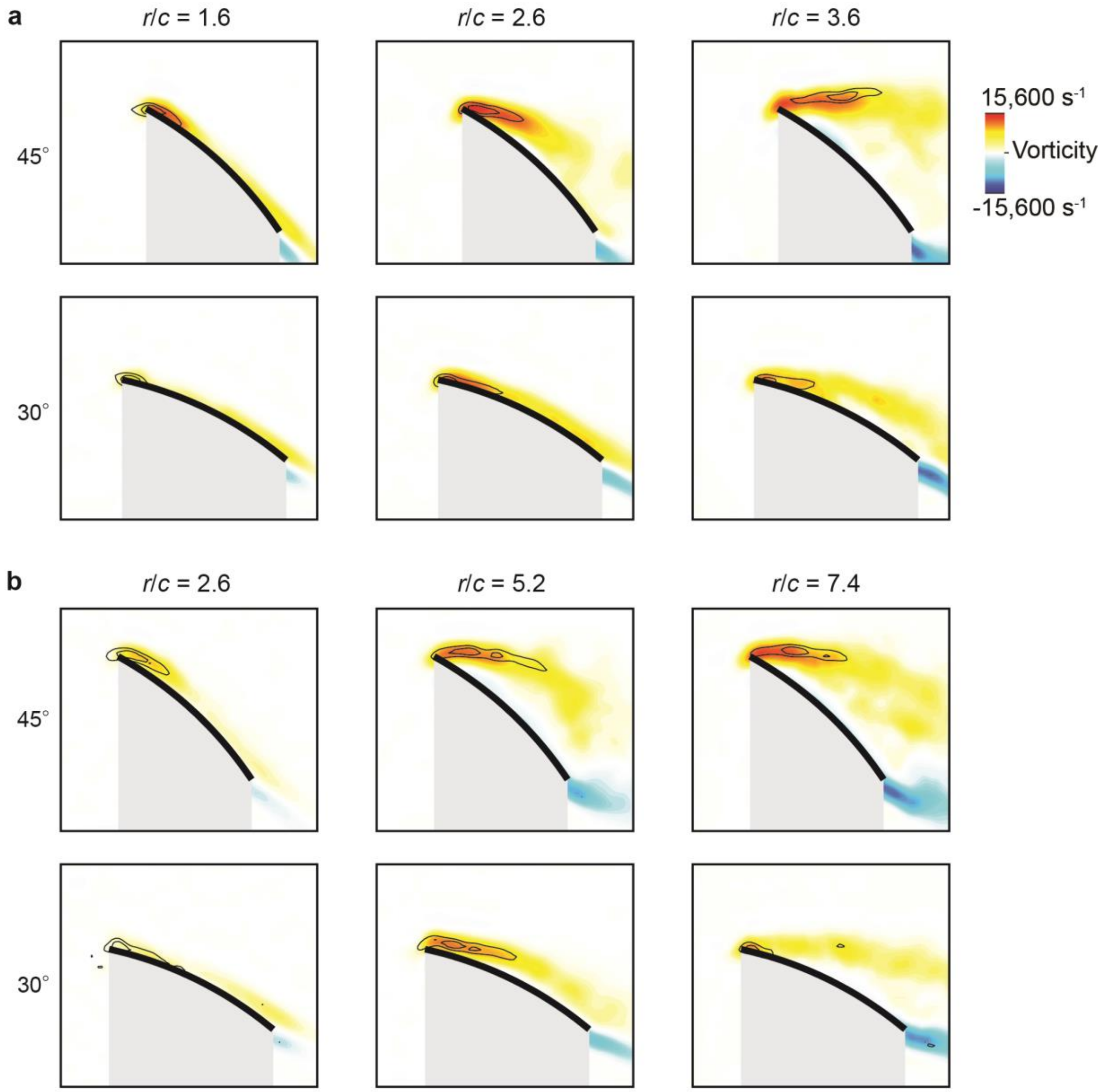

Figure S8. A non-local vortex detection scheme confirms that the leading edge vortex is either attached to, or tilted away from, the surface as a function of radial position r / c. The vortex identification results are similarly robust for (**a**), the aspect ratio 4 wing with $R/c = 4.6$ and (**b**), the aspect ratio 10 wing, with $R/c = 10.6$, at 30° and 45° incidence and $Re = 13{,}000$. The thin black contour lines represent a non-local scalar measure for axisymmetric vortex intensity ($\gamma = 0.4$ and $\gamma = 0.6$), which coincide with the peaks in the average local vorticity field (shown as color intensity in the background). Both the non-local vortex intensity and the local vorticity field show that the LEV is attached to the wing surface inboard (low r/c), and is detached from the surface outboard (high r/c). We thus conclude that our vorticity fields are sufficiently noise-free to detect vortices based on vorticity concentration. The thick black lines show the model wing cross-section; gray areas mask the area below the wing where the laser illumination was insufficient. The axisymmetric vortex intensity at a point P in the velocity field is defined as $\gamma(P) = \frac{1}{N}\sum \sin(\theta_M)$ following the work of Graftieaux *et al.*[14], which was implemented using MATLAB code from Jones *et al.*[13].

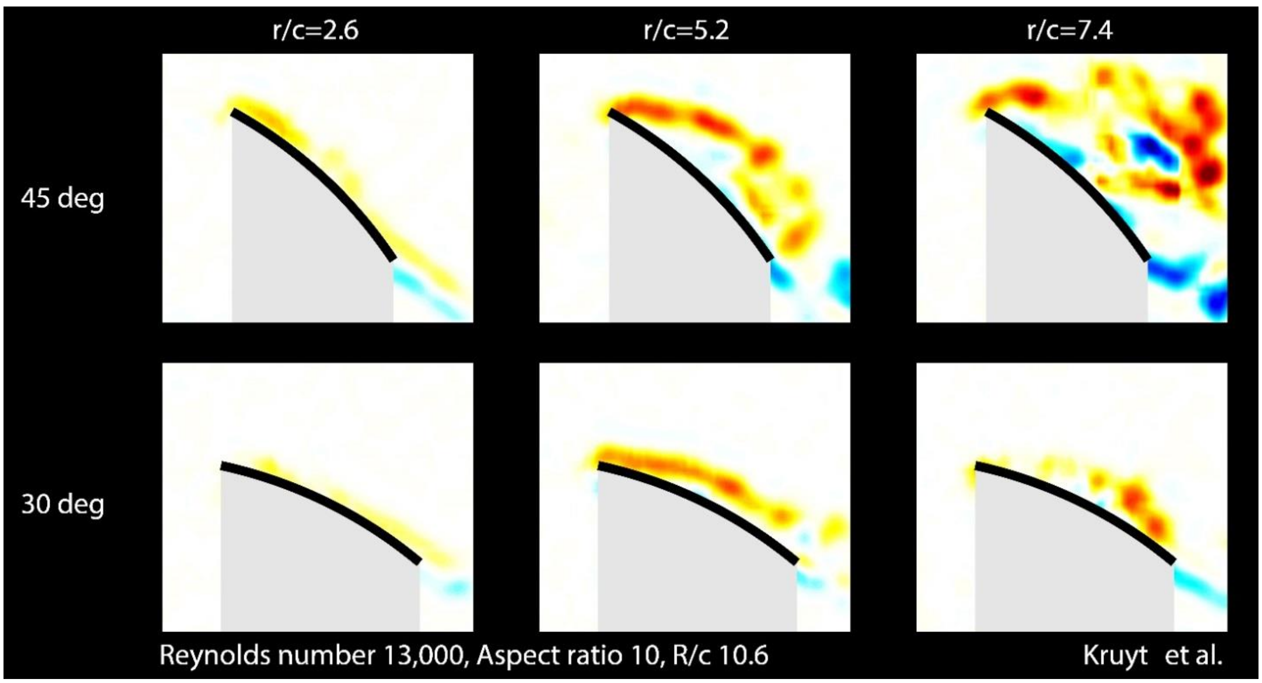

Movie S1 (still). Strong radial differences in LEV dynamics and flow separation are visible along the wing. The movie shows a loop of twenty instantaneous vorticity fields at three spanwise stations on an aspect ratio 10 model wing at 30° and 45° incidence. Inboard, the LEV is attached to the upper wing surface, whereas outboard vortex shedding and strong flow separation reveal the leading edge vortex is unsteady.

Cited References

1 Lentink, D. & Dickinson, M. H. Rotational accelerations stabilize leading edge vortices on revolving fly wings. *J Exp Biol* **212**, 2705-2719, doi:10.1242/jeb.022269 (2009).

2 Hein, B. R. & Chopra, I. Hover performance of a micro air vehicle: rotors at low Reynolds number. *Journal of the American helicopter Society* **52**, 254-262 (2007).

3 Bohorquez, F., Pines, D. & Samuel, P. D. Small rotor design optimization using blade element momentum theory and hover tests. *Journal of aircraft* **47**, 268-283 (2010).

4 Harbig, R., Sheridan, J. & Thompson, M. Reynolds number and aspect ratio effects on the leading-edge vortex for rotating insect wing planforms. *Journal of Fluid Mechanics* **717**, 166-192 (2013).

5 Altshuler, D. L., Dudley, R. & Ellington, C. P. Aerodynamic forces of revolving hummingbird wings and wing models. *Journal of Zoology* **264**, 327-332 (2004).

6 Weis-Fogh, T. Quick estimates of flight fitness in hovering animals, including novel mechanisms for lift production. *Journal of Experimental Biology* **59**, 169-230 (1973).

7 White, F. M. *Viscous Fluid Flow*. (McGraw-Hill, 1991).

8 Usherwood, J. R. & Ellington, C. P. The aerodynamics of revolving wings I. Model hawkmoth wings. *J Exp Biol* **205**, 1547-1564 (2002).

9 Usherwood, J. R. & Ellington, C. P. The aerodynamics of revolving wings II. Propeller force coefficients from mayfly to quail. *J Exp Biol* **205**, 1565-1576 (2002).

10 Wang, Z. J. Aerodynamic efficiency of flapping flight: analysis of a two-stroke model. *Journal of Experimental Biology* **211**, 234-238 (2008).

11 Eilers, P. H. A perfect smoother. *Analytical Chemistry* **75**, 3631-3636 (2003).

12 Poelma, C., Dickson, W. & Dickinson, M. Time-resolved reconstruction of the full velocity field around a dynamically-scaled flapping wing. *Experiments in Fluids* **41**, 213-225 (2006).

13 Jones, A., Pitt Ford, C. & Babinsky, H. Three-dimensional effects on sliding and waving wings. *Journal of Aircraft* **48**, 633-644 (2011).

14 Graftieaux, L., Michard, M. & Grosjean, N. Combining PIV, POD and vortex identification algorithms for the study of unsteady turbulent swirling flows. *Measurement Science and Technology* **12**, 1422 (2001).

15 Unal, M., Lin, J.-C. & Rockwell, D. Force prediction by PIV imaging: a momentum-based approach. *Journal of Fluids and Structures* **11**, 965-971 (1997).

16 Wu, J.-Z., Pan, Z.-L. & Lu, X.-Y. Unsteady fluid-dynamic force solely in terms of control-surface integral. *Physics of Fluids (1994-present)* **17**, 098102 (2005).

17 Dabiri, J. O. On the estimation of swimming and flying forces from wake measurements. *Journal of Experimental Biology* **208**, 3519-3532 (2005).

18 Van Oudheusden, B., Scarano, F. & Casimiri, E. Non-intrusive load characterization of an airfoil using PIV. *Experiments in fluids* **40**, 988-992 (2006).

19 Wu, J.-Z., Lu, X.-Y. & Zhuang, L.-X. Integral force acting on a body due to local flow structures. *Journal of Fluid Mechanics* **576**, 265-286 (2007).

20 Spedding, G. R. & Hedenström, A. PIV-based investigations of animal flight. *Experiments in Fluids* **46**, 749-763 (2009).

21 Van Oudheusden, B. PIV-based pressure measurement. *Measurement Science and Technology* **24**, 032001 (2013).

22 Mohebbian, A. & Rival, D. E. Assessment of the derivative-moment transformation method for unsteady-load estimation. *Experiments in fluids* **53**, 319-330 (2012).

23 Lentink, D., Dickson, W. B., van Leeuwen, J. L. & Dickinson, M. H. Leading-Edge Vortices Elevate Lift of Autorotating Plant Seeds. *Science* **324**, 1438-1440, doi:10.1126/science.1174196 (2009).